Available online at www.sciencedirect.com
SCIENCE DIRECT®
International Journal of Heat and Mass Transfer 48 (2005) 1450–1461
International Journal of HEAT and MASS TRANSFER
www.elsevier.com/locate/ijhmt

Experimental uncertainty of measured entropy production with pulsed laser PIV and planar laser induced fluorescence

O.B. Adeyinka, G.F. Naterer *

Department of Mechanical and Manufacturing Engineering, University of Manitoba, 15 Gillson Street, Winnipeg, Manitoba, Canada R3T 2N2

Received 9 April 2004; received in revised form 29 October 2004
Available online 13 December 2004

Abstract

The article develops an uncertainty analysis for a newly measured variable of local entropy production. Entropy production is measured with post-processing and spatial differencing of measured velocities from particle image velocimetry (PIV), as well as temperatures obtained from planar laser induced fluorescence (PLIF). Measurement uncertainties of fluid velocity depend on the time interval between laser pulses, width of the camera view and other factors. Bias errors are related to elementary bias components and sensitivity coefficients in the uncertainty analysis. The precision errors use a confidence coefficient of 2 for a 95% confidence interval. The newly developed measurement technique and uncertainty analysis are successfully applied to pressure-driven channel flow and buoyancy-driven free convection in a square enclosure.

1. Introduction

Uncertainty analysis involves systematic procedures for calculating error estimates for experimental data. When estimating errors in heat transfer experiments, it is usually assumed that data is gathered under fixed (known) conditions and detailed knowledge of all system components is available. Measurement errors arise from various sources, but they can be broadly classified as bias errors and precision (or random) errors. Bias errors remain constant during a set of measurements. They are often estimated from calibration procedures or past experience. Alternatively, different methods of estimating the same variable can be used, so that comparisons between those results would indicate the bias error. Elemental bias errors arise from calibration procedures or curve-fitting of calibrated data.

Also, ''fossilized'' bias errors arise when measuring and tabulating thermophysical properties. Although such errors are usually less than ±1%, Coleman and Steele [1] describe cases involving much higher levels of fossilized bias errors. Moffat [2] outlines a ''conceptual bias'', which includes a residual uncertainty due to variability arising in the true definition of the measured variable. For example, if point measurements are used to approximate bulk temperatures at the inlet and exit of a duct, then the difference between these temperatures and the bulk mean temperature contributes to a conceptual bias error, since point measurements cannot fully capture the spatially averaged bulk value.

In contrast to bias errors, precision errors appear through scattering of measured data. Such errors are

* Corresponding author. Tel.: +1 204 474 9804; fax: +1 204 275 7507.
E-mail address: natererg@cc.umanitoba.ca (G.F. Naterer).

0017-9310/$ - see front matter © 2004 Elsevier Ltd. All rights reserved.
doi:10.1016/j.ijheatmasstransfer.2004.10.021

Nomenclature

B	bias error	N	number of images
$\dot{P}_s$	entropy production rate (W/m^3 K)	x, y	Cartesian coordinates (m)
C_{max}	optimum concentration	P	precision error
Δs	particle displacement (μm)	X	general scalar variable
i, j	grid row and column number		
t	time(s), confidence coefficient	*Greek symbols*	
L_o	width of camera view (m)	ε	total error
T	temperature (K)	μ	dynamic viscosity (kg/ms)
L_I	width of digital image (m)	η	sensitivity coefficient
u, v	components of velocity (m/s)	σ	standard deviation of sample

affected by the measurement system (i.e., repeatability, resolution) or spatial/temporal variations of the measured quantity. Also, the procedure itself may lead to precision errors arising from variations in operating conditions. If an error can be estimated statistically, then it is usually considered to be a precision error. Otherwise, it is generally assumed to be a bias error. Anticipated precision errors are often used to guide experimental designs and procedures, in view of collecting data within a desired range of measurement uncertainty. Gui et al. [3] outline precision errors and other PIV measurement uncertainties in a towing tank experiment. Precision errors are reduced by increasing the number of measurement samples.

Alekseeva and Navon [4] find temperature uncertainties based on first and second order adjoint equations. An adjoint formulation of an inverse heat transfer problem leads to uncertainty indicators for the corresponding direct problem. Hessian maximum eigenvalues from the second order adjoint equations are used to evaluate the uncertainty indicators [4]. Pelletier et al. [5] show how sensitivity equations provide useful information regarding which parameters affect the flow response. Uncertainties are estimated with flow sensitivities, which are used to propagate parameter uncertainties throughout the domain. Applications to turbulent flow in an annular duct and conjugate free convection are considered [5]. Measurement uncertainties of flow parameters depending on input data errors (such as initial and boundary conditions) can be effectively calculated with adjoint equations. Alekseeva and Navon [6] use adjoint temperatures to calculate the transfer of uncertainties from such input data.

Spatial propagation of errors affects the overall experimental uncertainties. An individual error within an experiment combines with other errors, thereby leading to added uncertainty. Contributions can be evaluated separately with sensitivity coefficients involving the measured quantities and post-processed results, based on propagation equations [7]. Propagated uncertainties are often classified according to zero-order or higher-order uncertainties. In the former case, all parameters affecting the measurements are assumed to be fixed, except for the procedure of the experiment. Thus, data scattering arises from instrumentation resolution alone.

In the latter case (higher-order uncertainty), control of the experimental operating conditions is considered, so factors such as time are included. The degree of variability of operating conditions can be expressed by the standard deviation. The standard error of the mean describes how much variation of operating conditions is expected, when repeated samples from the same experiment are taken. It is the standard deviation of the mean, divided by a number characterizing the size of the sample. If this value is small, then there is large confidence in the measurement. But if the standard error of the mean is large, then either significant variations arise in the measurements, or the sample size was too small.

Measurement uncertainties of primary variables (such as fluid velocity) with various experimental techniques have been widely reported previously, i.e., Lassahn [8], Moffat [9], Kline [10] and others. Post-processing of measured data, such as measured vorticity from post-processed PIV data [11], entails additional uncertainties in the conversion algorithm. Unlike the primary variables with their governing conservation equations (equalities), entropy cannot be measured directly and it is governed by an inequality (Second Law of Thermodynamics). Entropy production can be expressed by either positive definite or transport forms [12,13]. Adeyinka and Naterer [14] define an apparent entropy production difference between these expressions, which gives useful insight regarding prediction errors. In this way, corrective steps can be taken to prevent non-physical trends in predictive models [15–17].

The purpose of this article is to determine how accurately entropy production can be measured with whole-field laser techniques involving PIV and PLIF. In particular, conventional error indicators [18] are

extended to the scalar variable of entropy production. Bias errors are related to sensitivity coefficients of the measured entropy production. The new measurement technique provides a useful way of improving energy efficiency in thermofluids engineering systems. Regions of highest measured entropy production can be targeted for purposes of system re-design, since they characterize flow losses from dissipated kinetic energy. These local rates of entropy production could be converted to local energy loss coefficients. In this way, local changes of a geometrical configuration, such as a modified turbine blade curvature, can be made to optimize the system efficiency.

Applications to pressure-driven channel flow and buoyancy-driven free convection in a square enclosure are documented in this article. But the new technique has valuable utility in other applications, ranging from aerospace to automotive, power generation, HVAC and others. For example, local entropy production within an aircraft diffuser can provide the designer with a systematic way of identifying and targeting areas incurring the most significant losses. Also, power generation devices (such as gas turbines) deliver maximum power output, while power consumption devices (i.e., compressors, pumps) consume the least power when the rate of entropy generation is minimized. Thus, iterative changes of a turbine blade profile, until entropy generation across the enclosed flow field is minimized, would yield the maximum power output and energy efficiency of the turbine. Another example is convective cooling of microelectronic assemblies, when each unit of entropy produced leads to a corresponding unit of heat flow which is desired to be removed, but cannot be removed due to entropy production. The irreversibilities lead to pressure losses within the enclosure and kinetic energy dissipated to internal energy, which works against the objective of cooling. In these applications, the newly developed method of whole-field measurement of entropy production is viewed to provide a useful method in reaching the maximum limits of energy efficiency.

2. Case (1): Channel flow

2.1. Experimental design

Experimental studies of channel flow are performed in a water tunnel with PIV (Particle Image Velocimetry) and 5 micron diameter polyamide seeding particles. A schematic of the experimental setup is illustrated in Fig. 1. The channel is 12.6 mm high, 60 cm wide and 2 m long. The measurements were performed at a Reynolds number of 518, based on the channel height and mean fluid velocity. The pulsed laser illuminates a planar cross-section in the center of the channel, parallel to the flow and perpendicular to the wall. Measurements were recorded sufficiently downstream of the channel inlet, so that fully developed conditions were obtained. The results represent an ensemble average of three different sets of velocity measurements with 1500 instantaneous images in each acquisition. The measured velocity profile was confirmed to be repeatable and steady over this time of data acquisition.

The PIV technique illuminates the seeding particles and the resulting camera images are used to analyze distances of particle group motion between images. The velocities can be obtained, after dividing the distance by the elapsed time of laser pulses. A Dantec 2100 PIV system, reflecting optics and two-chamber Gemini PIV Nd: Yag pulsed laser were used in this article. The PIV images were recorded with a Dantec HiSense CCD camera. The measured velocities are displayed

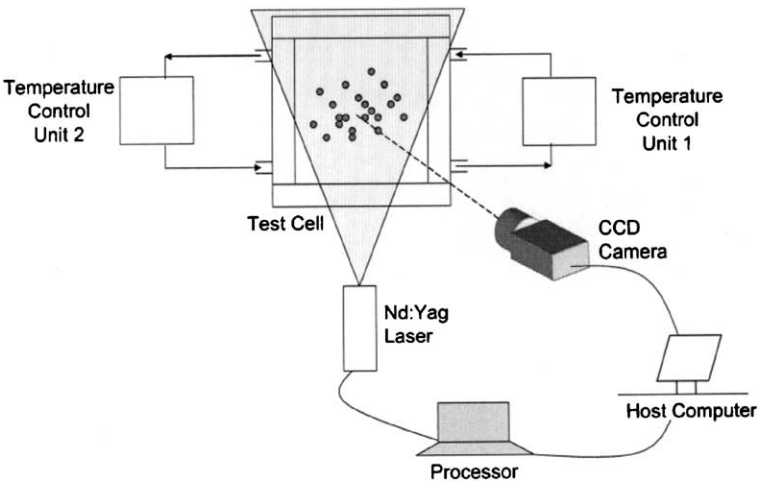

Fig. 1. Experimental setup.

over a discrete grid in the PIV software. The velocity components at grid position (i,j) are denoted by $u(i,j)$ and $v(i,j)$. The friction irreversibility of entropy production can be expressed by the viscous dissipation divided by temperature [12]. Thus, the local entropy production rate, $\dot{P}_s$, can be measured from

$$\dot{P}_s = \frac{\mu}{T(i,j)}\left(\frac{u(i,j+1)-u(i,j-1)}{\Delta y}+\frac{v(i+1,j)-v(i-1,j)}{\Delta x}\right)^2 + 2\frac{\mu}{T(i,j)}\left(\left(\frac{u(i+1,j)-u(i-1,j)}{\Delta x}\right)^2 + \left(\frac{v(i,j+1)-v(i,j-1)}{\Delta y}\right)^2\right) \quad (1)$$

where Δx and Δy refer to the grid spacing in the x and y directions.

2.2. Experimental uncertainties of measured entropy production

Since measured entropy production is a post-processed variable, the first step is assessing the experimental uncertainties of measured velocities. Unlike point-wise methods involving anemometry, Particle Image Velocimetry provides whole-field velocity measurements. But pulsed laser illumination and PIV incur certain errors from statistical correlations of the interrogation areas, when determining the fluid velocities.

For this problem of laminar channel flow, the average fluid velocity for an interrogation area at any instant is reduced by the following equation:

$$u = \frac{\Delta s L_o}{\Delta t L_I} \quad (2)$$

where Δt is the time interval between laser pulses, Δs is the particle displacement from the correlation algorithm, L_o is the width of the camera view in the object plane and L_I is the width of the digital image. The total error, ε, in a measured quantity is a sum of the bias component, B, and a precision component, P. The bias error of the measured velocity is related to the elementary bias errors based on the sensitivity coefficients, i.e.,

$$B_u^2 = \eta_{\Delta s}^2 B_{\Delta s}^2 + \eta_{\Delta t}^2 B_{\Delta t}^2 + \eta_{L_o}^2 B_{L_o}^2 + \eta_{L_I}^2 B_{L_I}^2 \quad (3)$$

where the sensitivity coefficients are defined as $\eta_\chi = \partial u/\partial \chi$. The manufacturer's specifications of the elementary bias limits $(\Delta t, \Delta s)$ are shown in Table 1. The width of the camera view in the object plane, L_o, depends on distances and configurations related to the experimental setup, so the bias limit for L_o is determined from calibration procedures, not manufacturer's specifications. In this calibration, the physical dimensions and spatial resolution of the camera view in the measurement plane are determined. Then the width of the digital image is determined by the number of pixels corresponding to these dimensions. In this problem, the width of the camera view in the object plane and bias limit for L_o are 0.0126 m and 0.0001, respectively. The uncertainty associated with this bias limit can be reduced with a more refined procedure for measurement of L_o.

The PIV image pairs are cross-correlated with a 32×32 interrogation window and 50% overlap. The time between pulses was chosen to ensure that the maximum displacement does not exceed a quarter of the side of the interrogation area. This yielded a Δs value of 6.4 pixels in the centerline. A HiSense CCD camera (1024×1018) fitted with a 35 mm lens and mounted on an extension ring (bellows) was used to capture pixels.

The measurement plane is $12.6\,\text{mm} \times 15.9\,\text{mm}$. Therefore, L_I and L_o are 1024 pixels and 12.6 mm, respectively. By combining the contributions of each bias error and the sensitivity coefficient, a velocity error of 0.76% is obtained for the full scale. The major source of velocity uncertainty occurs from locating the image displacement peak, Δs.

The precision error (P) of an average value, $\overline{X}$ measured from N samples is given by

$$P = \frac{t\sigma}{N} \quad (4)$$

where t is the confidence coefficient and σ is the standard deviation of the sample of N images. Also, t equals 2 for a 95% confidence level [19]. The standard deviation is defined as follows:

Table 1
Bias errors (case 1)

Variable, X	Magnitude	B_x	η_x	$B_x\eta_x$	$B_x\eta_x/\sum B_x\eta_x$	$(B_x\eta_x)^2$
L_o (m)	1.26E−02	0.0001	4.13E+00	4.13E−04	58.8	1.71E−07
L_I (pixel)	1024	0.5	−5.09E−05	2.54E−05	3.6	6.47E−10
Δt (s)	1.50E−03	0.0000001	−3.47E+01	3.47E−06	0.5	1.21E−11
Δs (pixel)	6.35	0.03175	8.20E−03	2.60E−04	37.1	6.78E−08
				$\sum B_x\eta_x = 7.03\text{E}-04$	$B_u = 0.0005$	
					Bias error = 0.0645 ± 0.7586%	

$$\sigma = \sqrt{\frac{1}{N-1}\sum_{k=1}^{N}(X_k - \overline{X})^2} \tag{5}$$

The average quantity is defined by the following equation:

$$\overline{X} = \frac{1}{N}\sum_{k=1}^{N} X_k \tag{6}$$

Typical values of the standard deviation along the centerline and the near-wall region are 15% and 33%, respectively. These values give precision limits of 0.67% and 1.55% for those regions. Therefore, the total uncertainty of measured velocity in the middle of the channel and the near-wall region become 1.4% and 2.2%, respectively.

Based on these results, the errors of measured entropy production can be estimated. A data reduction equation for entropy production is given by

$$\dot{P}_s = \frac{\mu}{T}\left(\frac{\Delta u}{\Delta y}\right)^2 + \frac{k}{T}\left(\frac{\Delta T}{\Delta y}\right)^2 \tag{7}$$

The total uncertainty ($B + P$) for the u, T and y variables are

$$u_i = \bar{u}_i \pm \varepsilon_{u_i} \tag{8}$$

$$T_i = \overline{T}_i \pm \varepsilon_{T_i} \tag{9}$$

$$y_i = \bar{y}_i \pm \varepsilon_{y_i} \tag{10}$$

The uncertainty in Δu is obtained as follows:

$$\varepsilon_{\Delta u} = \pm\sqrt{(\theta'_{u,i+1}\varepsilon_{u,i+1})^2 + (\theta'_{u,i-1}\varepsilon_{u,i-1})^2} \tag{11}$$

where

$$\theta'_{u,i-1} = \frac{\partial(\Delta u)}{\partial u_i} \tag{12}$$

Note that $\theta'_{u,i-1} = -1$ and $\theta'_{u,i+1} = 1$ or vice versa. The uncertainty of ΔT is calculated in the same manner as Eqs. (11) and (12), except that the velocity component, u, is replaced by temperature, T. In the upcoming results, the analytical solution of entropy production is derived from differentiation of the Poiseuille velocity profile for laminar channel flows, thereby leading to the frictional irreversibility in the first term on the right side of Eq. (7). This solution neglects temperature variations, since the experiment was conducted between unheated plexiglass plates in an essentially isothermal water tunnel. However, the frictional irreversibility dissipates kinetic energy to internal energy, which produces a small temperature change in the boundary layer near the walls. The uncertainty corresponding to this measured temperature change is reported in Table 2, based on the procedure outlined in Eqs. (11) and (12).

Similarly,

$$\varepsilon_{\Delta y} = \pm\sqrt{(\theta'_{y,i+1}\varepsilon_{y,i+1})^2 + (\theta'_{y,i-1}\varepsilon_{y,i-1})^2} \tag{13}$$

where

$$\theta'_{y,i-1} = \frac{\partial(\Delta y)}{\partial y_i} \tag{14}$$

Neglecting the error in reported thermophysical properties,

$$\varepsilon^2_{P_s} = \eta^2_T\varepsilon^2_T + \eta^2_{\Delta u}\varepsilon^2_{\Delta u} + \eta^2_{\Delta y}\varepsilon^2_{\Delta y} + \eta^2_{\Delta T}\varepsilon^2_{\Delta T} \tag{15}$$

Based on this equation and the previous procedure of individual uncertainties, it was determined that the experimental uncertainty of entropy production was 11.67% at a point of 3 mm from the bottom wall.

But less error was observed when analytical results were compared with measured data (agreement within ±6.6% close to the wall). The measurement uncertainties represent a maximum error bound within the 95% confidence interval. Detailed calculations of the experimental uncertainties are summarized in Tables 1 and 2.

2.3. Results and discussion

The accuracy of the entropy production algorithm was validated by comparing the measured values of velocity and entropy production to an analytical

Table 2
Bias and precision errors of entropy production at y = 1.7 mm (Case 1)

Variable, X	Magnitude	ε_x	η_x	$\varepsilon_x\eta_x$	$\varepsilon_x\eta_x/\sum\varepsilon_x\eta_x$	$(\varepsilon_x\eta_x)^2$
u (m/s)	0.0345	0.00013453	0	0	0.0	0
y (m)	0.0126	0.000001	0	0	0.0	0
T (K)	295	2	−3.3466E−06	6.7E−06	5.3	4.4799E−11
μ (kg/ms)	0.001003	0	3.1459E−03	0	0.0	0
k (W/mk)	0.5996	0	0	0	0.0	0
Δu (m)	0.00336544	0.00019026	5.8670E−01	0.00011	89.0	1.246E−08
Δy (m)	0.0001975	1.4142E−06	−4.9987E+00	7.1E−06	5.6	4.9975E−11
ΔT (K)	0	2.82842712	0	0	0.0	0
				1.25E−04	ε_u = 0.000112	
					Error = 0.00095268 ± 11.76%	

solution for laminar channel flow [14]. The analytical solution is referenced to the measured maximum velocity in the channel. In Fig. 2, the differences between analytical and measured results are generally less than ±1.2%. A maximum difference of 6.6% between the measured entropy production and the analytical result occurs close to the wall. The location of this maximum error is not unexpected, in view of PIV limitations due to particle tracking, camera resolution and a reduced number of seeding particles in each interrogation region near the wall.

In Fig. 2a, the velocity reaches a maximum value at the centerline. Velocity measurements at different distances downstream (i.e., 110 cm and 110.6 cm from the inlet) were recorded. Close agreement between measured velocities at both points confirms that fully developed flow behavior was reached. The zero gradient of velocity at the centerline leads to a zero measured entropy production in Fig. 2b. Since there is zero shear stress across the mid-plane of the channel due to symmetry, this corresponds to zero kinetic energy dissipated to internal energy.

A closer view of the near-wall entropy production is shown in Fig. 3. The entropy production rises in the cross-stream (y) direction to its peak value at the wall, but does not change noticeably in the streamwise (x) direction, due to fully developed conditions. After multiplying entropy production by temperature in Fig. 3, those results give the destruction of exergy (or energy availability in the flow stream). This conversion allows units to be expressed directly in terms of lost power per unit volume of fluid, which can be more practically interpreted than units of lost power per degree Kelvin (units of entropy production).

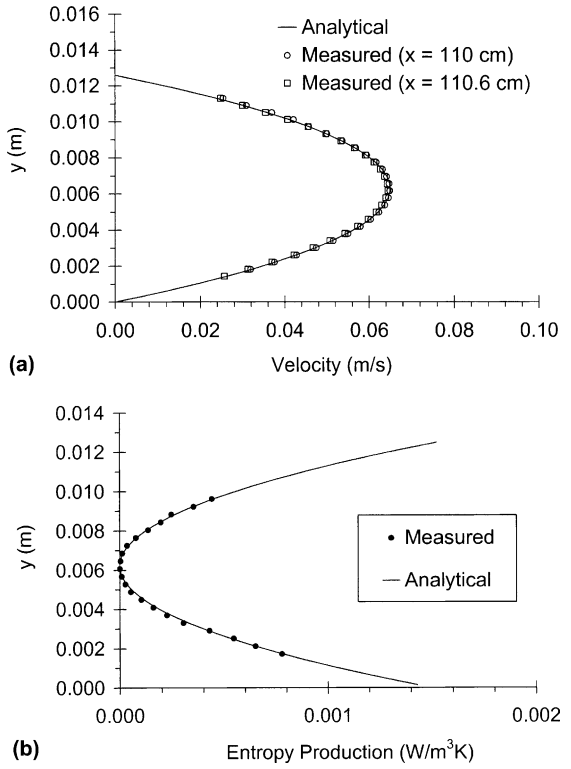

Fig. 2. Analytical and measured (a) velocity and (b) entropy production (channel flow).

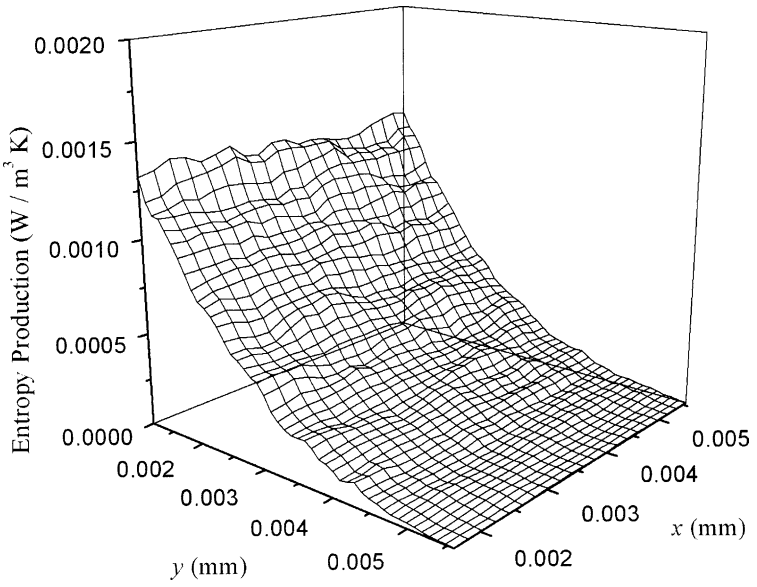

Fig. 3. Surface plot of measured near-wall entropy production (channel flow).

3. Case (2): Free convection heat transfer

3.1. Experimental design

Unlike pressure-driven flow in the previous problem, this second problem considers entropy production with buoyancy-driven flow and free convection in a 39 mm square cavity (see Fig. 4). In this problem, the test cell in Fig. 1 was constructed with two Aluminum multi-pass heat exchangers at the side walls, connected to temperature control units (NESLAB RTE140 circulators). Also, 17.5 mm plexiglass windows were assembled on the bottom, top, back and front faces. The 59 mm depth of the test cell was considered to have small three-dimensional variations of temperature and velocity fields.

Initial calibration was performed with distilled water, which was seeded with a solution of Rhodamine B at a known concentration and temperature. The vertical plane of symmetry was illuminated from above by the Nd:Yag pulsed laser. Concentration and temperature calibrations were performed for the PLIF measurements. Spatial variations of temperature are needed in the post-processed calculations of measured entropy production.

A basis of PLIF technology is that molecules and atoms emit light in a de-excitation process induced by absorption of a photon of higher energy. The local fluorescence intensity, I, varies with concentration of the fluorescent dye, quantum efficiency and other variables. Calibration for the current experiments indicates that the intensity, I, decreases monotonically with respect to temperature, T, at a fixed rate (see Fig. 5). Preliminary calibrations were carried out at a fixed energy level to determine the optimum concentration, C_{max}, at which the resolution of the temperature field is maximum while maintaining linearity between intensity and temperature. This concentration was found to be 15 μg of Rhodamine B per liter of water in the present work. In the final calibration shown in Fig. 5, the concentration was fixed at approximately 89% of the optimum concentration (i.e., $C_o = 0.89 \times C_{max} = 13.5$ μg/l) while two energy levels were considered to account for the response of every pixel of the camera to varying laser energy levels.

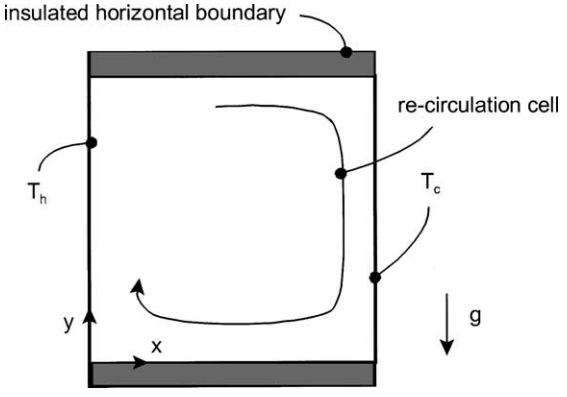

Fig. 4. Problem schematic.

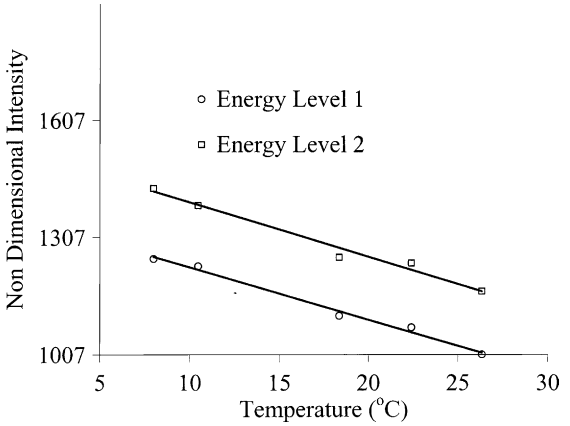

Fig. 5. PLIF calibrated intensity at varying temperatures (°C).

A CCD camera was used to capture both PLIF and PIV images, with optical filters switched for sequential measurements. In this problem, the 1024×1018 pixel PIV image plane of the camera was divided into 32×32 pixel sub-regions with 50% overlap to give a spatial resolution of 0.7 mm. The system was operated in a double frame mode with 100 ms delay time between successive frames. In the experiments, the PLIF images were re-sampled by a calibration map with a spatial resolution corresponding to the velocity map. Based on the PIV velocity measurements and PLIF temperature measurements, the same conversion algorithm (described previously in Section 2) for frictional entropy production was applied.

In the experimental studies, PLIF measurements were performed to determine temperatures in the denominator of the entropy production in Eq. (1). For this buoyancy driven problem, the temperature field varies spatially, thereby affecting the frictional entropy production in Eq. (1). The non-intrusive technique of pulsed laser PIV was used for whole-field measurements of velocity, which were post-processed by spatial differencing in the frictional entropy generation of Eq. (1). Thus, a similar whole-field non-intrusive technique (Planar Laser Induced Fluorescence) was used for the temperature measurements, rather than thermocouples or other intrusive probes. Constructing a grid with probe locations that match all (i,j) coordinates corresponding to the discrete PIV grid in Eq. (1) would be infeasible and it would lack flexibility over a useful range of applications.

3.2. Experimental uncertainties of measured entropy production

A similar procedure (as Section 2; near-isothermal channel flow) was adopted for the bias and precision

errors, but with certain differences due to variations of temperature within the enclosure. Unlike the previous channel flow problem, friction irreversibilities in this problem vary spatially due to both velocity and temperature variations across the flow field. For this problem, the bias error of the measured velocity is related to the elementary bias errors and sensitivity coefficients as follows:

$$B_u^2 = \eta_{\Delta s}^2 B_{\Delta s}^2 + \eta_{\Delta t}^2 B_{\Delta t}^2 + \eta_{L_o}^2 B_{L_o}^2 + \eta_{L_I}^2 B_{L_I}^2 \tag{16}$$

where the same definition of sensitivity coefficients is used, i.e., $\eta_\chi = \partial U/\partial \chi$. By combining the contributions from each source of bias and the sensitivity coefficient, a full-scale velocity bias error of 0.45% is obtained.

Similarly as previously described, the precision error (P) of an average value, $\overline{X}$, measured from N samples and the standard deviation are given by

$$P = \frac{t\sigma}{N} \tag{17}$$

$$\sigma = \sqrt{\frac{1}{N-1}\sum_{k=1}^{N}(X_k - \overline{X})^2} \tag{18}$$

where the average quantity is

$$\overline{X} = \frac{1}{N}\sum_{k=1}^{N} X_k \tag{19}$$

Typical values of the standard deviation at the points of maximum velocity and near the wall are 0.5% and 1.2%, respectively. These values yield precision limits of 0.005% and 0.012%, respectively. Therefore, the total uncertainties of measured velocity at these points are 0.45% and 0.5%, respectively.

For this free convection problem, the data reduction equation for friction irreversibility of entropy production becomes

$$P_s = \frac{\mu}{T}\left\{\left(\frac{\Delta u_y}{\Delta y}\right)^2 + \left(\frac{\Delta v_x}{\Delta x}\right)^2 + \left(\frac{\Delta u_x}{\Delta x}\right)^2 + \left(\frac{\Delta v_y}{\Delta y}\right)^2\right\} \tag{20}$$

The same definitions are applied from the previous problem, including the total uncertainties for the u, T, Y, Δu and Δy variables. Then, the total uncertainty of entropy production becomes

$$\varepsilon_{P_s}^2 = \eta_T^2 \varepsilon_T^2 + \eta_{\Delta u}^2 \varepsilon_{\Delta u}^2 + \eta_{\Delta v}^2 \varepsilon_{\Delta v}^2 + \eta_{\Delta y}^2 \varepsilon_{\Delta y}^2 \tag{21}$$

For this problem of free convection, the total uncertainty of measured entropy production was estimated to be 9.34% at $X = 0.985L$ and $Y = 0.46L$, where L refers to the cavity height. This estimate represents a maximum error bound within the 95% confidence interval. Tables 3 and 4 show the summarized calculations of the experimental uncertainties for this problem of free convection in an enclosure.

The uncertainty of temperature measurements is included in the overall uncertainty of entropy production. This total uncertainty is represented in terms of precision and bias components, with sensitivity coefficients involving the PLIF temperature measurements (see Table 4). Although the total entropy production includes friction and thermal irreversibilities, this article focuses on the friction irreversibility component. This component includes velocity gradients and measured temperatures in the denominator, while the thermal component involves temperature gradients in the flow field. Since the uncertainties of measured temperatures are small compared to the magnitude of the absolute temperature in the denominator, the sensitivity coefficient of temperature in the uncertainty analysis is small. Based on parameters outlined in Table 4, the sensitivity coefficient for temperature is 5.0×10^{-9}. The maximum error in the PLIF temperature measurements (ε_T) becomes ±5 °C. This error is combined with others in the total uncertainty of entropy production, including measured velocity gradients in the flow field. These results are summarized in Table 4. In these results, the dynamic viscosity has been evaluated at a uniform temperature (288 K). Variations of the dynamic viscosity, due to changes or errors in the measured temperatures, have been neglected in the uncertainty analysis.

3.3. Results and discussion

In this section, measured data and experimental errors involving the free convection problem will be presented. The measured entropy production will be

Table 3
Bias error (Case 2)

Variable, X	Magnitude	B_x	η_x	$B_x\eta_x$	$B_x\eta_x/\sum B_x\eta_x$	$(B_x\eta_x)^2$
L_o (m)	7.00E−03	0.0001	6.51E−02	6.51E−06	61.8	4.24E−11
L_I (pixel)	1024	0.5	−4.45E−07	2.23E−07	2.1	4.95E−14
Δt (s)	9.00E−02	1E−07	−5.06E−03	5.06E−10	0.0	2.56E−19
Δs (pixel)	6	0.05	7.60E−05	3.80E−06	36.1	1.44E−11
				$\sum B_x\eta_x$ = 1.05E − 05	B_u = 7.5404E−06	
					Bias error = 1.67E−03 ± 0.4515%	

Table 4
Bias and precision errors for case 2 (entropy production; $x = 0.985L$, $y = 0.46L$)

Variable, X	Magnitude	ε_x	η_x	$\varepsilon_x\eta_x$	$\varepsilon_x\eta_x/\Sigma\varepsilon_x\eta_x$	$(\varepsilon_x\eta_x)^2$
u (m/s)	−4.56E−05	−2.06E−07	0	0	0.0	0.00E+00
v (m/s)	−1.37E−03	−6.20E−06	0	0	0.0	0.00E+00
x (m)	7.00E−03	0.0000001	0	0	0.0	0.00E+00
y (m)	6.80E−03	0.0000001	0	0	0.0	0.00E+00
T (K)	288	5	−5.00E−09	2.5016E−08	0.0	6.26E−16
μ (kg/ms)	1.14E−03	0	1.27E−03	0	0.0	0.00E+00
k (W/mk)	0.5911	0	0	0	0.0	0.00E+00
Δu_x (m/s)	−2.6033E−06	2.90905E−07	0.17365	5.0515E−08	0.1	2.55E−15
Δv_x (m/s)	0.000191341	8.76872E−06	6.38156	5.5958E−05	79.6	3.13E−09
Δu_y (m/s)	−1.3016E−06	2.90905E−07	0.04341	1.2629E−08	0.0	1.59E−16
Δv_y (m/s)	−5.2065E−06	8.76872E−06	-0.34730	3.0453E−06	4.3	9.27E−12
Δx (m)	0.0000154	1.41421E−07	−79.31843	1.1217E−05	16.0	1.26E−10
Δy (m)	0.0000154	1.41421E−07	0.12109	1.7124E−08	0.0	2.93E−16
				$\sum\varepsilon_x\eta_x = 7.03\text{E}-05$	$\varepsilon = 0.000057$	
					Error = 6.1168E−04 ± 9.34%	

compared against predicted results from a Control-Volume Based Finite Element Method [14]. Results are presented from an 80×80 mesh (grid independent resolution, based on grid refinement studies). Detailed information regarding the numerical formulation of entropy production is documented in Ref. [14]. Also, validation of predicted temperatures, velocities and Nusselt numbers was performed by comparisons against benchmark results of de Vahl Davis [20].

The measured velocities indicated that a single clockwise re-circulation cell developed with highest velocities near the side walls. The fluid velocities diminish rapidly at locations further from the wall, so that velocities become too small for PIV vectors to be displayed in the central region of the cavity. In Figs. 6 and 7, the u-velocity and v-velocity along the vertical and horizontal mid-planes, respectively, are illustrated, In each case, the velocities are non-dimensionalized with respect to the maximum velocity, while the spatial coordinate is non-dimensionalized with respect to the cavity width.

Close agreement between predicted and measured results is achieved in Figs. 6 and 7. The velocity is non-dimensionalized with respect to a measured maximum velocity of 1.69 mm/s. The measured velocity field is slightly skewed to the right side of the cavity, so some discrepancy between predicted and measured results is observed near the right wall. The numerical simulation assumes a perfectly insulated boundary on both horizontal walls of the cavity, which leads to complete symmetry without skewing of the velocity field. The experimental apparatus closely approaches this idealization, but any slight heat gains through the horizontal boundaries could potentially lead to asymmetry of the buoyancy-driven flow. Experimental uncertainties discussed in the previous section are considered to have contributed to the slight skewing of the measured veloc-

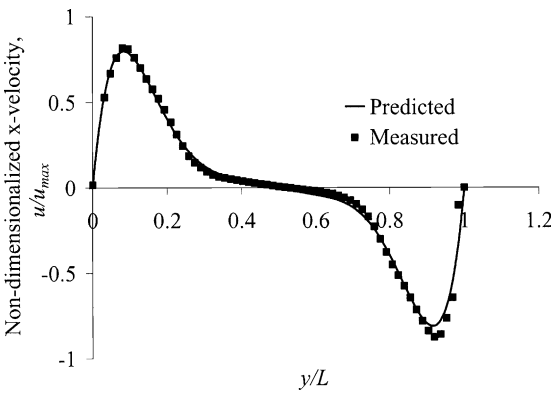

Fig. 6. u-Velocity on vertical mid-plane ($Ra = 5.35 \times 10^6$, $Pr = 8.06$).

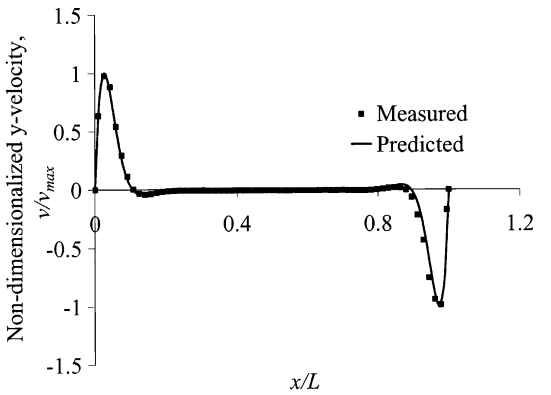

Fig. 7. v-Velocity on horizontal mid-plane ($Ra = 5.35 \times 10^6$, $Pr = 8.06$).

ity to the right in Fig. 6. In Fig. 7, very close agreement between measured and predicted results is obtained. Velocity measurements close the wall were obtained (within 1 mm from the wall), due to their importance in subsequent spatial differencing for entropy production at the wall. Both Figs. 6 and 7 exhibit nearly symmetrical profiles of velocity along the mid-planes of the cavity.

Fig. 8 illustrate the horizontal mid-plane predicted and measured results of entropy production. The entropy production increases to peak values at the center of each side wall. Away from these points, entropy production decreases sharply to approximately zero close to the wall, which corresponds to the local maximum and zero gradient of v-velocity near the wall in Fig. 7. Beyond this local maximum of velocity, entropy production increases to a local maximum ($\dot{P}_{S_{ref}}$) and decreases back to nearly zero in the central region of the enclosure. The result presented in Fig. 8 has been normalized with a reference entropy production at this local maximum. The entropy production reaches a minimum value in the center of the cavity, where the stagnation point of the re-circulation cell is observed. Close agreement between qualitative trends of predicted results and measured entropy production is observed in Fig. 8. But greater oscillations of measured entropy production are observed closer to the wall, when the whole cavity is captured, due to limitations of camera resolution. Due to the importance of these near-wall irreversibilities, additional entropy production measurements, obtained by resolving the velocity field closer to the wall, are shown in Fig. 8. The associated uncertainties are summarized in Tables 3 and 4.

In addition to certain levels of discretization error in the numerical simulations (Fig. 8), various limitations of PIV technology are encountered at the wall. These limitations involve the particle tracking algorithm, camera resolution and particles contained within the near-wall interrogation regions. Such limitations have considerable impact on measured velocity, with even more substantial effects on entropy production, since it entails spatial gradients of velocity at the wall. Errors of measured velocity are magnified to larger errors of entropy production, when differences of velocity over small distances are used. Such magnified errors lead to oscillations of measured whole field data in Fig. 8. The previously reported measurement uncertainties are evaluated at 0.8 mm from the wall, so they may not be directly applicable within 0.2 mm to the wall, where the current PIV technology may be incapable of fully resolving spatial gradients of velocity.

Measured oscillations of entropy production can be effectively reduced through filtering of velocity data. In Fig. 9, a 3×3 average filter was used for smoothing of the raw velocity vectors, before calculating entropy production. Previous PIV studies [11] have shown that filtering does not introduce additional error into the measured velocity, but it serves to mitigate uncertainty by averaging velocities at surrounding grid points. Fig. 9 shows the measured velocity distribution with the corresponding filtered profile at the horizontal mid-plane. The results illustrate the benefit of filtering, particularly for the near-wall raw data points and removing random uncertainty in the measured velocity gradients.

Additional near-wall measurements of velocity and entropy production are presented in Figs. 10 and 11. In Fig. 10, water accelerates as it flows downward along the cold wall, when its density exceeds warmer fluid further away from the wall. As a result, the near-wall velocity gradient and resulting friction irreversibility become higher, so the entropy production increases in that direction (see Fig. 11). The results presented in Figs. 10 and 11 have been normalized with the reference velocity and entropy production, respectively. Since entropy production in Fig. 11 is normalized with respect to a reference entropy production (value of local maximum on horizontal mid-plane) and entropy production decreases along the right vertical boundary, the non-dimensional entropy production takes on values larger than one. Measured entropy production provides a useful tool for designers, when tracking local losses of flow irreversibility or exergy (energy availability).

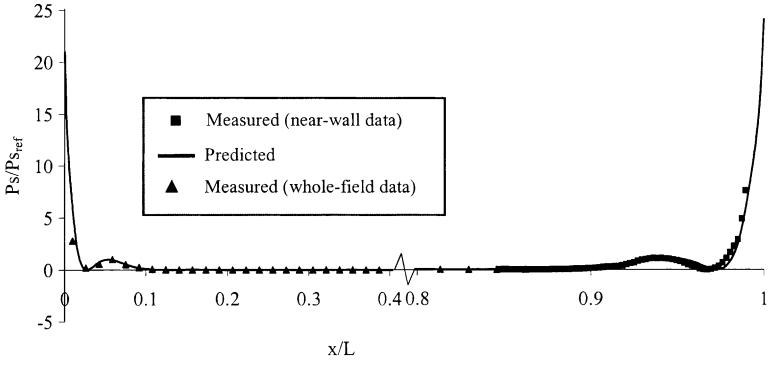

Fig. 8. Horizontal mid-plane results ($Ra = 5.35 \times 10^6$, $Pr = 8.06$).

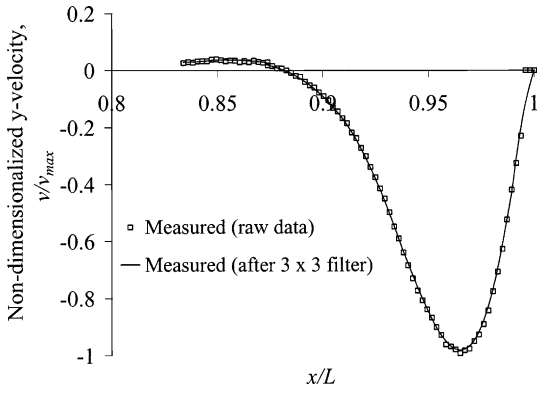

Fig. 9. Filtering of velocity profile ($Ra = 5.35 \times 10^6$, $Pr = 8.06$).

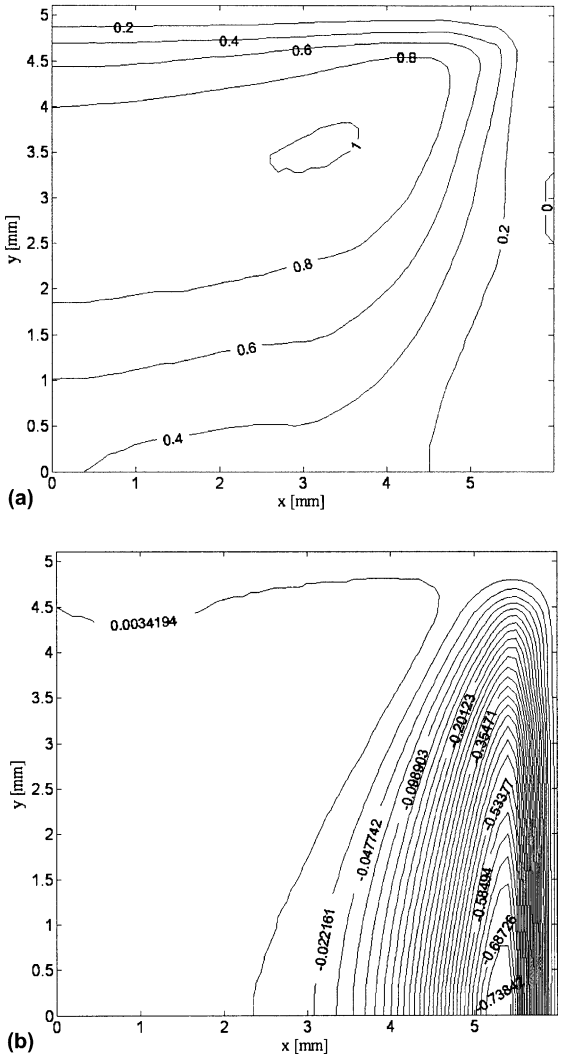

Fig. 10. Near-wall measured velocities (top-right corner at cold wall); (a) u/u_{max}; (b) v/v_{max}.

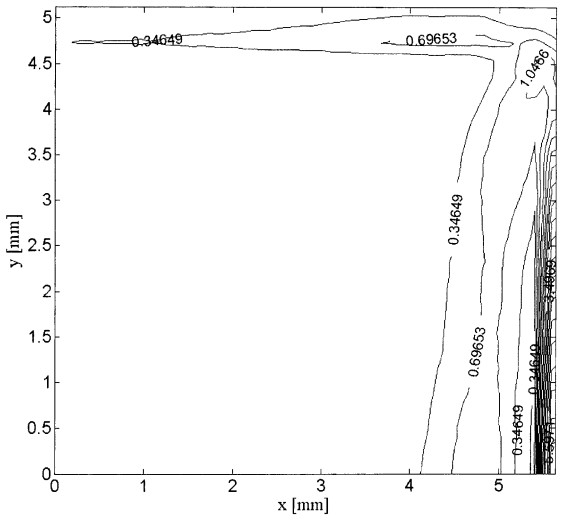

Fig. 11. Near-wall measured $P_s/P_{s,ref}$ (top-right corner at cold wall).

Such measurements are considered to have practical utility in various applications. An example is mixed convective cooling of microelectronic assemblies (involving both forced and free convection). Each unit of exergy destroyed represents a certain desired heat flow which may have been removed, but was not removed, due to irreversible conversion of kinetic energy to internal energy (i.e., undesirable temperature rise). Such dissipation is characterized by the local entropy production rate, which contributes to a higher pressure loss and reduced effectiveness of forced convection during cooling of the entire assembly. This example represents only a single application. The newly developed method of entropy production measurement and uncertainty analysis are considered to have significance in various other technological applications.

4. Conclusions

Newly developed procedures are presented for wholefield measurement and uncertainty assessment of entropy production. Measured velocities and temperatures are obtained by methods of Particle Image Velocimetry (PIV) and Planar Laser Induced Fluorescence (PLIF). A conversion algorithm is developed with post-processing of the measured variables, so that spatial variations of entropy production can be determined. Measurement uncertainties involve total bias, elementary bias contributions and precision errors. For laminar channel flow between parallel plates, the values of standard deviation in the velocity along the centerline and near-wall region are 15% and 33%, respectively. Near the wall, a precision limit of 1.55% and total uncertainty of 2.4% are

reported. For the problem of free convection in an enclosure, the measurement uncertainty of entropy production is 9.34%, based on a maximum error bound within the 95% confidence interval. Peak values of entropy production are measured near the centers of the side walls, due to high spatial gradients perpendicular to the wall at those locations. Measured entropy production is considered to have considerable practical utility as a diagnostic tool, when tracking local losses of energy availability due to the thermofluid irreversibilities.

Acknowledgments

This work was supported by a research grant from the Natural Sciences and Engineering Research Council of Canada to G.F. Naterer, as well as a University of Manitoba Graduate Fellowship (O.B. Adeyinka). Also, infrastructure support from CFI (Canada Foundation for Innovation) and WED (Western Economic Diversification) is gratefully acknowledged.

References

[1] H.W. Coleman, W.G. Steele, Experimentation and Uncertainty Analysis for Engineers, Wiley, 1989.
[2] R.J. Moffat, Describing the uncertainties in experimental results, Exp. Thermal Fluid Sci. 1 (1988) 3–17.
[3] L. Gui, J. Longo, F. Stern, Towing tank PIV measurement system, data and uncertainty assessment for DTMB Model 5512, Exp. Fluids 31 (2001) 336–346.
[4] A.K. Alekseeva, M.I. Navon, On estimation of temperature uncertainty using the second order adjoint algorithm, Int. J. Comput. Fluid Dyn. 16 (2) (2002) 113–117.
[5] D. Pelletier, E. Turgeon, D. Lacasse, J. Borggaard, Adaptivity, sensitivity and uncertainty: toward standards of good practice in computational fluid dynasmics, AIAA J. 41 (10) (2003) 1925–1933.
[6] A.K. Alekseeva, I.M. Navon, Calculation of uncertainty propagation using adjoint equations, Int. J. Comput. Fluid Dyn. 17 (4) (2003) 283–288.
[7] S.J. Kline, F.A. McClintock, Describing uncertainties in single-sample experiments, Mech. Eng. 75 (1953) 3–8.
[8] G.D. Lassahn, Uncertainty definition, ASME J. Fluids Eng. 107 (1985) 179.
[9] R.J. Moffat, Contributions to the theory of single-sample uncertainty analysis, ASME J. Fluids Eng. 104 (1982) 250–260.
[10] S.J. Kline, The purpose of uncertainty analysis, ASME J. Fluids Eng. 107 (153–160) (1985).
[11] J.D. Luff, T. Drouillard, A.M. Rompage, M.A. Linne, J.R. Hertzberg, Experimental uncertainties associated with particle image velocimetry (PIV) based vorticity algorithms, Exp. Fluids 26 (1999) 36–54.
[12] G.F. Naterer, Heat Transfer in Single and Multiphase Systems, CRC Press, Boca Raton, FL, 2002.
[13] G.F. Naterer, Constructing an entropy-stable upwind scheme for compressible fluid flow computations, AIAA J. 37 (3) (1999) 303–312.
[14] O.B. Adeyinka, G.F. Naterer, Apparent entropy difference with heat and fluid flow irreversibilities, Numer. Heat Transfer B 42 (2002) 411–436.
[15] G.F. Naterer, J.A. Camberos, Entropy and the second law in fluid flow and heat transfer simulation, AIAA J. Thermophys. Heat Transfer 17 (3) (2003) 360–371.
[16] G.F. Nellis, J.L. Smith, Entropy-based correction of finite difference predictions, Numer. Heat Transfers B 31 (2) (1997) 177–194.
[17] G.F. Naterer, G.E. Schneider, Use of the second law for artificial dissipation in compressible flow discrete analysis, AIAA J. Thermophys. Heat Transfer 8 (3) (1994) 500–506.
[18] AIAA-Standard-S017-1995, Assessment of Experimental Uncertainty with Application to Wind Tunnel Testing. American Institute of Aeronautics and Astronautics, 1995.
[19] H.W. Coleman, W.G. Steele, Engineering application of experimental uncertainty analysis, AIAA J. 33 (1995) 1888–1896.
[20] G. De Vahl Davis, Natural convection of air in a square cavity: a Benchmark solution, Int. J. Numer. Meth. Fluids 3 (1983) 249–264.